Senseable City Lab :.:: Massachusetts Institute of Technology

This paper might be a pre-copy-editing or a post-print author-produced .pdf of an article accepted for publication. For the definitive publisher-authenticated version, please refer directly to publishing house's archive system

Urban Forestry & Urban Greening 126 (2026) 129708

Contents lists available at ScienceDirect

Urban Forestry & Urban Greening

journal homepage: www.elsevier.com/locate/ufug

Original article

Greenery Scanner: A drive-by platform for urban greenery NDVI sensing using low-cost multispectral camera

Leonardo Iacussi [a,b,1], Song Guo [a,d,1], Simone Mora [a,f,*], Andrei Speridĩao [a], Oluwatobi Oyinlola [a], Giancarlo Papitto [e], Umberto Fugiglando [a,c], Paolo Chiariotti [b], Alfredo Cigada [b], Carlo Ratti [a,c]

[a] Senseable City Lab, Massachusetts Institute of Technology, 77 Massachusetts Avenue, Cambridge, MA, USA
[b] Department of Mechanical Engineering, Politecnico di Milano, Piazza Leonardo da Vinci 32, Milan, 20133, Italy
[c] Department of Architecture, Built Environment and Construction Engineering, Politecnico di Milano, Via privata Giuseppe la Masa 1, Milan, 20156, Italy
[d] School of Architecture, Tsinghua University, Beijing, 100084, China
[e] Carabinieri Command of Forestry, Environmental and Agri-food Units (CUFA), Rome, 00187, Italy
[f] Department of Computer Science, Norwegian University of Science and Technology, Hogskoleringen, Trondheim, 7491, Norway

ARTICLE INFO

Keywords:
Urban tree health monitoring
Street-level remote sensing
Crown dieback assessment
Urban forest management
NDVI
Drive-by sensing
Near-Infrared (NIR) Image

ABSTRACT

Urban trees provide environmental, social, and economic benefits, but they are increasingly affected by biotic and abiotic stressors. Frequently updated tree-health inventories are therefore essential for proactive urban greenery management. Aerial and satellite multispectral imaging can support tree-health assessment through the Normalized Difference Vegetation Index (NDVI), but in dense urban environments these approaches may be limited by canopy occlusions, top-down viewing perspective, operational costs, and revisit constraints. Street-level multispectral imaging offers a complementary perspective by capturing lower and lateral canopy portions that may contain stress signals invisible from the above. This study proposes a method for street-level urban greenery monitoring, enabled by Greenery Scanner (GS): an open-source, low-cost, drive-by platform. The approach combines vehicle-mounted multispectral sensing nodes with an AI-based processing pipeline that segments tree canopy pixels from panoramic images and extracts calibrated NDVI values. We use the platform for crown dieback detection in *Pinus pinea* trees in Rome, Italy, where canopy decline is primarily associated with infestation by *Toumeyella Parvicornis*. A laboratory experiment measured the functional and radiometric consistency of GS against a Spectralon target with a mean NIR/R ratio of 1.037 and an NDVI residual error of 0.018 under controlled illumination. A field deployment on 84 trees showed that GS-derived NDVI was significantly associated with arborist-assessed crown dieback severity ($p < 0.01$). The data was used to feed a binary logistic classifier distinguishing severe (≥50%) from early/low dieback (<50%) achieving 66% accuracy. We discuss how GS can support prioritizing arborist inspections, complementing and enhancing existing methods.

1. Introduction

Urban forests provide important environmental, social, and economic benefits, including air pollutant removal, carbon sequestration, urban temperature regulation, and enhancement of human well-being (Viecco et al., 2018; Baldocchi et al., 2018; Ziter et al., 2019; Reyes-Riveros et al., 2021). They produce health benefits valued at approximately $4.7 billion per year (Nowak et al., 2014) the US alone. Despite their many benefits, urban forests face increasing pressure from both biotic and abiotic stressors. Environmental factors such as water scarcity, soil compaction, physical damage, poor pruning, air pollution, and vehicle collisions weaken trees, while pests, pathogens, and diseases threaten an estimated 40% of woody biomass (Cavender-Bares et al., 2022). Urban expansion further exacerbates these impacts, with the US. tree canopy declining by about 175,000 acres annually, which is equivalent to the loss of 36 million trees and $96 million in ecosystem benefits each year (Nowak and Greenfield, 2018). These trends highlight the urgent need for scalable, cost-effective approaches to support tree inventories and monitor urban tree condition, enabling early detection and intervention (Dowtin et al., 2023).

* Corresponding author at: Senseable City Lab, Massachusetts Institute of Technology, 77 Massachusetts Avenue, Cambridge, MA, USA.
E-mail address: moras@mit.edu (S. Mora).
[1] These authors contributed equally to this work.

https://doi.org/10.1016/j.ufug.2026.129708
Received 8 April 2026; Received in revised form 21 July 2026; Accepted 19 September 2026
Available online 30 September 2026
1618-8667/© 2026 Elsevier GmbH. All rights are reserved, including those for text and data mining, AI training, and similar technologies.

Visual and instrumented assessments by arborists are widely regarded as the most reliable methods for evaluating urban tree health. However, they are labor-intensive and time-consuming, limiting scalability and resulting in high-quality but spatially sparse observations (Koeser et al., 2017). Given the extent and dynamic nature of urban green infrastructure, these assessments benefit from complementary approaches that can screen large areas and support the prioritization of field inspections (Gupta et al., 2024a). Existing methods partially address this need but involve trade-offs. Unmanned Aerial Vehicle (UAV) surveys, using drone-mounted multispectral cameras to map tree health from an aerial view through NDVI or related spectral indices, provide high spatial resolution but are constrained by costs and regulations (Näsi et al., 2018). Satellite imagery enables large-scale monitoring but suffers from coarse resolution, cloud interference, and limited revisit times (Lausch et al., 2016). Tree-mounted sensors offer high temporal resolution but are costly and difficult to scale (Torresan et al., 2021). Together, these approaches highlight trade-offs between coverage, resolution, cost, and operational complexity. In particular, none of these approaches provides frequent street-level observations capable of capturing lower-canopy condition signals at scale, which is the gap this work aim to fill.

A complementary strategy to address these trade-offs is the integration of environmental sensors into vehicles, commonly referred to as drive-by sensing (Anjomshoaa et al., 2018). By leveraging existing fleets (e.g., taxis or mail delivery vehicles), this approach enables rapid coverage of large urban areas. Repeated passes along the same road segments introduce temporal redundancy and data consistency, supporting frequent, bottom-up observations and improved robustness (Mora et al., 2019).

Previous studies have demonstrated the effectiveness of this paradigm for urban environmental monitoring, including applications in air quality assessment (Wang et al., 2023a) and urban heat characterization (Merdymshaeva et al., 2025), with platforms deployed on vehicles such as road maintenance fleets and taxis (Wang et al., 2023b). Applied to urban greenery, drive-by sensing offers a street-level perspective well suited to assessing tree conditions, complementing both arborist field inspections and top-down airborne observations.

This research aims at investigating whether NDVI data from low-cost, multispectral imagery captured from a ground-up perspective in a drive-by condition can provide meaningful indicators of tree health and how this data can complement existing survey methods. To this goal, we introduce *Greenery Scanner* (GS) an open-source platform for drive-by monitoring of urban greenery. GS combines low-cost multispectral environmental sensors, with an AI-based data analysis pipeline to segment urban greenery and compute the Normalized Difference Vegetation Index (NDVI) from tree crown pixels. By relying on inexpensive, off-the-shelf components, the platform is designed to support broad deployment scenarios, enabling more frequent and spatially extensive assessments of urban vegetation conditions.

The platform is evaluated on a specific tree-health monitoring application: the detection of crown dieback in *Pinus pinea* trees in Rome, Italy, where canopy decline is primarily associated with infestation by *Toumeyella parvicornis*. This application is particularly relevant for street-level sensing because crown dieback may affect lower and lateral canopy portions that are visible from roads but less directly observable from top-down aerial imagery. A preliminary laboratory experiment under controlled illumination was first conducted to verify the functional and radiometric consistency of the GS sensor, custom optical configuration, calibration palette, and image-processing workflow on a neutral Spectralon reference target. This test was used only as a pre-deployment consistency check, rather than as a comprehensive validation of outdoor measurement accuracy. The main validation and performances on detecting trees affected by the infestation was then performed through a field deployment in Rome, where GS-derived street-level NDVI was compared with expert crown-dieback assessments for *Pinus pinea* trees. We aim at discussing how data collected from GS can complement arborists' visual assessments and NDVI data collected by UAV to provide an holistic evaluation of tree health.

This work provides the following contributions:

1. an open-source, low-cost drive-by sensing platform for bottom-up urban greenery monitoring,
2. a calibration and visual-AI processing pipeline for extracting canopy-level NDVI from multispectral street-level imagery,
3. an application-specific validation demonstrating how GS-derived NDVI relates to arborist-assessed crown dieback severity in *Pinus pinea* trees in an urban environment in Rome, Italy.
4. evidences of how GS-derived NDVI can complement and extend existing methods

By releasing both the source code and fabrication instructions, the platform is intended to support reproducible research and future deployments across different urban greenery monitoring use cases.

2. Related work and technologies

Tree health monitoring increasingly relies on non-contact, imaging-based approaches due to their efficiency and non-invasiveness (Gupta et al., 2024a). These approaches can be broadly organized according to their sensing perspective. Airborne and spaceborne platforms, such as UAVs and satellites, provide top-down observations over large areas, while terrestrial and street-level platforms acquire imagery from the viewpoint of pedestrians, vehicles, and urban infrastructure. Across these perspectives, vegetation monitoring commonly relies on visible and near-infrared (NIR) spectral information, because healthy vegetation exhibits strong NIR reflectance (Knipling, 1970). As a result, the Normalized Difference Vegetation Index (NDVI), derived from NIR (750–1000 nm) and red (600–750 nm) reflectance, is one of the most widely used indices to assess vegetation condition (Xue and Su, 2017).

2.1. Airborne and spaceborne vision-based sensing for greenery monitoring

Airborne and spaceborne imaging have become widely used for vegetation and tree-health monitoring because they can provide spatially extensive observations from a top-down perspective. Hyperspectral imaging captures a large number of narrow spectral bands that enable detailed analysis of plant spectral signatures beyond the computation of vegetation indices (Näsi et al., 2018; Stuart et al., 2022). The availability of dense spectral information allows the investigation of specific wavelength regions associated with physiological processes and stress responses, improving the detection and discrimination of plant pathologies and conditions (Faqeerzada et al., 2025). However, hyperspectral systems are typically employed in laboratory or controlled illumination settings, where acquisition conditions can be carefully managed (Balios et al., 2026). Their applicability in outdoor, large-scale drive-by urban scenarios is limited by several factors, such as the relatively long acquisition times required to form a single image, their high cost (thousands of USD), and the amount of data to manage (up to GBs for each frame) (Fernandez-Figueroa et al., 2021).

Multispectral cameras, on the other hand, acquire only a limited number of spectral bands, typically targeting those most relevant for vegetation analysis, such as the red and near-infrared bands. By relying on simpler sensor architectures, including low-cost CMOS sensors combined with optical band-pass filters, they offer reduced cost (hundreds of USD), lower data throughput, and faster acquisition times, making them more suitable for outdoor sensing applications. Their use is already established in precision agriculture and vegetation monitoring using multispectral cameras installed on UAVs. For example, Gomes et al. (2021) showed that a single-sensor camera with suitable optical filters and calibration can produce NDVI values statistically consistent with those from conventional multi-sensor systems in coffee crops. In Bahe et al. (2021), a single miniature camera has been proven

efficient for detecting stress in deciduous juvenile tree foliage in a controlled environment. These characteristics make multispectral imaging a pragmatic compromise between spectral information content, system complexity, and operational scalability for vegetation monitoring.

2.2. Terrestrial and street-level vision-based sensing for greenery monitoring

Terrestrial and street-level sensing approaches provide a complementary vision-based perspective to airborne and spaceborne remote sensing for urban greenery monitoring. While top-down imagery primarily captures the upper canopy, street-level observations record vegetation from the viewpoint of pedestrians, vehicles, and urban infrastructure. This viewpoint is particularly relevant in dense urban environments, where buildings, narrow streets, and overlapping crowns can limit the interpretability of overhead imagery and where lower and lateral canopy portions may contain condition signals that are not visible from above. A substantial body of work has used street-level RGB imagery, especially Google Street View and other mobile-mapping image sources, to quantify urban greenery attributes. Early studies introduced image-based indicators such as the Green View Index to measure the amount of visible greenery along streets (Li et al., 2015). More recent approaches have applied deep learning and semantic segmentation to estimate tree presence, canopy cover, green-view metrics, and structural categories (Khan et al., 2021; Zhang et al., 2023). These methods are valuable because they provide spatially detailed, human-scale information along road networks and can exploit large existing image repositories. However, they mainly rely on visible-spectrum imagery and therefore describe appearance, structure, or visual exposure rather than directly measuring spectral vegetation indices such as NDVI, which require near-infrared information. Beyond image repositories, vehicle-based sensing platforms have been explored as a way to acquire terrestrial observations of urban vegetation and environmental conditions at scale. Mobile mapping systems commonly integrate panoramic cameras, LiDAR, and GNSS/INS sensors to reconstruct urban scenes and support georeferenced analysis (Lu et al., 2025). For green infrastructure monitoring, Fuentes et al. (2021) mounted visible and thermal infrared cameras on a moving vehicle to assess tree-level growth and water-status-related indicators, demonstrating the potential of vehicle-based sensing for operational urban vegetation monitoring. Similarly, Gupta et al. (2024b) investigated mobile terrestrial sensing for urban tree-health assessment by combining thermal and multispectral imaging with computer vision methods. These studies show that vehicles can act as scalable sensing platforms by repeatedly sampling road-accessible urban greenery. Overall, terrestrial and street-level approaches offer clear advantages for urban greenery monitoring, including human-scale observation, access to lower and lateral canopy portions, and compatibility with repeated acquisitions along road networks. At the same time, most existing street-level studies are based on RGB imagery, while systems incorporating near-infrared or multispectral sensing remain comparatively limited. This leaves an open methodological challenge: acquiring reliable street-level spectral measurements under uncontrolled outdoor illumination, while separating tree crowns from complex urban backgrounds and associating canopy pixels with meaningful vegetation-health indicators. These challenges motivate the calibration, segmentation, and validation procedures described in the following sections.

Across both top-down and street-level sensing paradigms, recent image-based AI methods have been increasingly used to automate tree-health monitoring tasks. For example, convolutional Neural Network (CNN) models have been trained on UAV, satellite, street-view, and multi/hyperspectral images to classify tree health indices (Kagan et al., 2021; Dash et al., 2018; Chi et al., 2020). Transfer learning methods such as *ResNet* and *EfficientNet* have proven effective in detecting leaf diseases (Padshetty and Ambika, 2023; Hanh et al., 2022). Open-source AI libraries like *YOLO* have been applied for real-time pest detection (Liu et al., 2023). Semantic segmentation approaches, such as *U-Net* and *Deeplab V3*, enable the delineation of individual tree crowns (Wang et al., 2024). While these AI-based methods demonstrate the potential of automated vegetation analysis, their performance in low-cost and real-world implementations remains constrained by illumination variability, viewpoint limitations, and mismatch between curated training datasets and operational urban scenarios. These limitations are particularly relevant for drive-by street-level acquisition, where segmentation and NDVI extraction must operate under changing lighting, complex backgrounds, and non-standard viewing geometries.

3. Materials and methods

The methodology adopted in this work is organized around two main components. First, the Greenery Scanner (GS) was designed and implemented as a low-cost drive-by hardware and software platform (sub 1000 USD) for acquiring multispectral imagery and auxiliary environmental data from conventional vehicles. Second, an image calibration and segmentation pipeline was developed to process the acquired multispectral images, isolate tree crowns in urban environments, and compute NDVI values from the masked canopy pixels. The GS platform is released open-source under the MIT License and available on Github.[2] We position GS as a complementary approach to existing methods, particularly suited to applications requiring a bottom-up perspective and repeated measurements enabled by drive-by deployment, such as detecting early changes in NDVI associated with emerging biotic or abiotic stressors.

3.1. Greenery scanner sensing platform

The GS combines a low-cost multispectral camera with location and auxiliary environmental sensors, including air temperature, relative humidity, and particulate matter (PM). The use of commercially available, low-cost components was a key design constraint, aimed at supporting large-scale deployments and cost-effective replication of the system. A primary design objective was ease of deployment, enabling the platform to be operated by non-expert users without prior experience in embedded systems. The sensing node is conceived as a self-contained unit that can be directly mounted on a vehicle using embedded magnetic feet and controlled through a smartphone-based interface (see Fig. 1(e)). Fig. 2 presents an exploded view of the GS, highlighting its main structural and functional components. The primary components labeled in the figure are described below.

The multispectral camera **(d)** is the core component of the GS, as it enables the acquisition of spectral information in the Red, Green, and Near-Infrared (RGN) bands required to compute vegetation indices, including NDVI. In this study, the MAPIR Survey 3 RGN multispectral camera was used. This imaging sensor has been widely adopted in the literature for NDVI estimation (Lozoya et al., 2019; Muliady. et al., 2022). The camera is based on a single 1/2.3″ CMOS sensor and acquires RAW images using a three-band RGN optical filter configuration. The manufacturer-provided firmware maps the acquired signal into red, green, and near-infrared channels, with nominal band centers at 660 nm, 550 nm, and 850 nm, respectively. The manufacturer datasheet reports narrow filter responses around these centers, with an effective bandwidth of approximately 50 nm per band. These bands are directly relevant to NDVI estimation, which relies on the red and near-infrared channels. A key design requirement arising from the operation of the GS under drive-by conditions was to achieve multispectral coverage of urban greenery on both sides of the vehicle while minimizing hardware complexity and cost. To this end, the node employs a single multispectral sensor, thereby avoiding the need for multiple synchronized cameras. To maximize spatial coverage, the

[2] https://github.com/MIT-Senseable-City-Lab/greenery-scanner.

Fig. 1. Device to be mounted on the top of a vehicle (a), calibration targets (b), battery (c), battery charger (d), user interface web application (e).

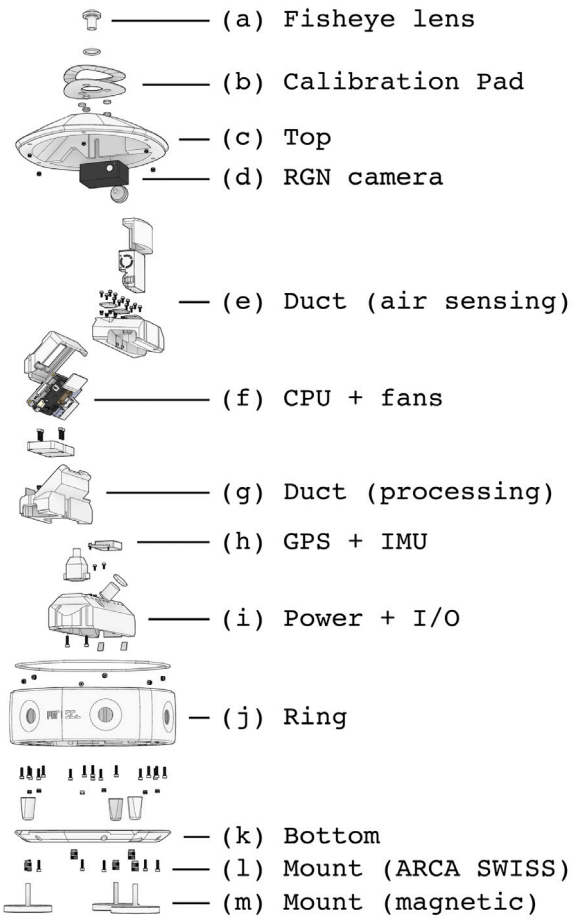

Fig. 2. Exploded view of the Greenery Scanner sensing node. Detailed sensor specifications, 3D-printed part files, fabrication instructions, and the complete bill of materials are provided in the GitHub repository cited in the text.

multispectral camera is oriented upward and coupled with a custom-made fisheye lens **(a)**. This configuration enables a 360-degree field of view around the vehicle. The selected fisheye lens provides an angular field of view of 225 degrees, which is sufficient to capture the majority of street-level urban greenery within a traffic lane. The lens uses an M12 threaded mount compatible with the MAPIR Survey3 optical interface and was customized for multispectral acquisition by replacing the standard infrared-cut filter, typically used in lenses for CMOS (Complementary Metal-Oxide-Semiconductor) sensors, with a manufacturer-provided RGN optical filter. The custom filter was selected to reproduce the nominal MAPIR Survey3 RGN spectral configuration, preserving the red, green, and near-infrared bands used for NDVI estimation.

The central section of the device houses a removable battery compartment **(i)**, which ensures balanced weight distribution and allows for rapid battery replacement. An integrated CPU **(g)**, based on the Raspberry Pi 4B Compute Module (Raspberry Pi Ltd, 2025), supports data acquisition, storage, and interaction with the smartphone-based user interface. Due to the computational load associated with continuous data acquisition, the device incorporates an active ventilation system consisting of two cooling fans **(f)**: one fan draws ambient air into the enclosure, while the other expels warm air to prevent overheating. Each GS also includes a GPS module and an Inertial Measurement Unit (IMU) **(h)** to enable geo-tagging and time-stamping of the collected data. The system includes a CEVA BNO085 inertial measurement module (CEVA-IP, 2025) for vehicle orientation estimation, operating in conjunction with a GPS chip (MAPIR, 2025a) to provide reliable positioning and motion information.

In addition, the GS integrates environmental sensors **(e)** to monitor ambient conditions, including temperature, relative humidity, and particulate matter. These sensors are strategically positioned away from the computational unit **(g)** to minimize thermal interference. Although they are not required for NDVI estimation, they are included to support future applications and enable potential correlation analyses across heterogeneous data sources.

The external enclosure **(k)** ensures mechanical stability during vehicle motion while protecting the internal components. Its design accommodates additional sensing modules, such as extra cameras, through dedicated slots **(j)**, thereby enabling future extensions of the platform. The enclosure can be 3D-printed using domestic-grade printers, with fabrication instructions provided in our open-source release. The device can be mounted on ordinary vehicles, such as cars and trucks, using either three 1/4″ magnetic mounts **(m)** or a 120 mm ARCA-SWISS standard mount **(l)**. User interaction and data management are supported through an illuminated on/off power button, which provides operational feedback, and an RJ-45 Ethernet port for data transfer and system configuration. The mobile application allows users to start and stop acquisition sessions and to monitor system status in real time, including sensor operation, battery level, and available storage. (Fig. 1(right)). A firmware automatically launches at startup, synchronizing image acquisition with environmental sensor readings and GPS-based location and time. The RGN camera maximum frame rate limits capture frequency to one RAW image every five seconds. After each data collection experiment, the user can transfer collected datasets via WiFi

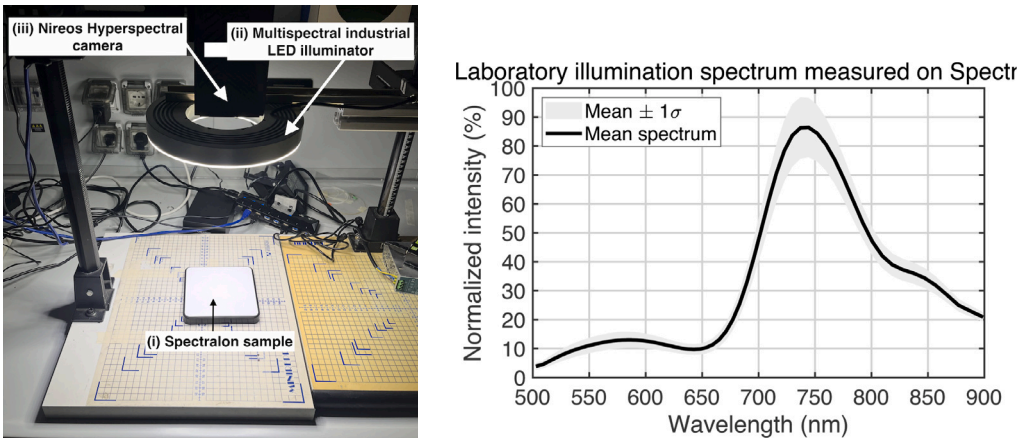

(a) (b)

Fig. 3. (a) Laboratory acquisition setup for calibration palette characterization. The three main components are annotated: (i) the Spectralon white reference standard (Labsphere, Inc, 2024), with known 99% diffuse reflectance, used for absolute reflectance reference; (ii) the circular multispectral LED ring illuminator (Genesi Elettronica, 2025), providing uniform controlled illumination over the target surface; and (iii) the Nireos VNIR hyperspectral camera (Nireos, 2025), positioned vertically above the sample at a fixed working distance. (b) Normalized spectral distribution of the laboratory illumination measured on the Spectralon white reference.

or wired connection using the Secure File Transfer Protocol (SFTP). The firmware also takes care of real-time communication of essential information to the user interface (Fig. 1(e)). For details on the implementation of GS sensing node and full part list, please refer to the GS GitHub repository.[3]

3.1.1. Reflectance characterization of calibration materials

Extracting NDVI values from drive-by street images poses several challenges. Light conditions vary constantly due to weather and surrounding structures, affecting camera exposure and white balance. The fisheye lens with its 225-degree field of view creates optical distortions such as lens flare, chromatic aberration, and vignetting, causing inconsistent spectral responses across the image. To obtain accurate reflectance measurements in the red and NIR bands needed for NDVI calculation, we have designed an onboard calibration target (a gray-leveled palette with felt materials providing varying reflectance levels) that appears in every image alongside the environment, as shown in Fig. 1(b). Positioned around the fisheye lens, this target remains visible in all frames and angles within the 360° panoramic image. This setup enables the restoration of each picture by applying corrections tailored to different sections of the panorama.

The reflectance properties of the felt materials used in the calibration target were characterized in a controlled laboratory setting using a Spectralon sample (Labsphere, Inc, 2024) as a reference (see Fig. 3). To obtain calibration curves for the four felt materials (white, light gray, dark gray, and black) a Nireos VNIR hyperspectral camera (Nireos, 2025) with 120 spectral bands (400–1000 nm) has been used along with an industrial multispectral LED illuminator (Genesi Elettronica, 2025). The spectral distribution of the illumination used during the experiment was characterized on the Spectralon white reference and is shown in Fig. 3(b). The measured spectrum confirms the presence of radiance across the wavelength range relevant to the RGN camera channels, with a pronounced contribution in the near-infrared region used for NDVI estimation. Subsequent reflectance estimates were normalized with respect to this measured illumination spectrum, and the LED illuminator output was kept constant through its internal controller throughout the experimental session. The reflectance curve and corresponding correction matrix for each material is obtained by averaging reflectance values across three points per sample. To reduce noise, each hyperspectral image has been created by averaging five consecutive captures. The noise floor of the sensor was recorded and used as a black reference, allowing the reflectance values of the target materials to be calibrated and normalized, as follows (Cruz-Guerrero et al., 2022):

$$\hat{\mathbf{I}}(x,y,n) = 100 \times \frac{\mathbf{I}_{\text{raw}}(x,y,n) - \mathbf{R}_{\text{B}}(x,y,n)}{\mathbf{R}_{\text{W}}(x,y,n) - \mathbf{R}_{\text{B}}(x,y,n)}, \tag{1}$$

considering $\hat{\mathbf{I}}$ the calibrated hyperspectral (HS) image, $\mathbf{R}_{\text{B}}$ as the black reference HS image, and $\mathbf{R}_{\text{W}}$ as the white reference HS image. x and y are the numbers of pixels of the images and n the number of spectral bands considered in the acquisition.

Fig. 4(b) shows the normalized reflectance curves of the four materials, presented as percentage values averaged from the area of interest (x_{sample}, y_{sample}). The RGN camera filters (MAPIR, 2025b) have been modeled as Gaussian functions centered at 660 nm (Red), 550 nm (Green), and 850 nm (NIR), with standard deviations from the MAPIR camera datasheet.

The expected reflectance of each calibration material in each camera channel was then computed by integrating the product of the simulated filter response and the measured material reflectance curve over the relevant wavelength range, normalized by the filter response integral:

$$M_{m,c} = \frac{\int_{\lambda} F_c(\lambda)\, \rho_m(\lambda)\, \mathrm{d}\lambda}{\int_{\lambda} F_c(\lambda)\, \mathrm{d}\lambda}, \tag{2}$$

where $\rho_m(\lambda)$ is the measured reflectance curve of material m (white, light gray, dark gray, or black), $F_c(\lambda)$ is the Gaussian filter response of channel c (Red, Green, or NIR), and $M_{m,c}$ is the resulting calibration matrix entry reported in Table 1. This procedure was applied independently to each of the three camera channels, yielding the complete calibration matrix used for per-image reflectance correction during drive-by acquisition.

3.2. Image processing

The image processing pipeline (Fig. 5) serves three purposes: (i) to perform white balance correction using the calibration targets pixel values, (ii) to isolate tree canopy pixels from the background, and

[3] https://github.com/MIT-Senseable-City-Lab/greenery-scanner.

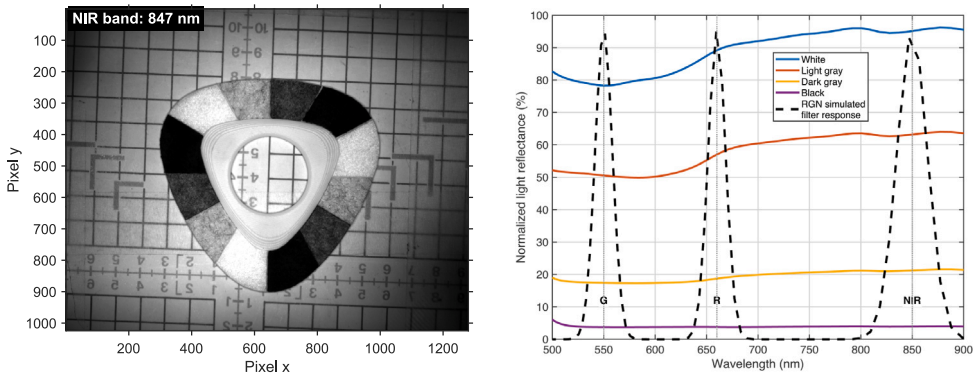

Fig. 4. **(a)** Example hyperspectral image of the calibration palette in the near-infrared band at 850 nm. **(b)** Reflectance curves of the calibration palette materials and simulated RGN camera filter response used to derive the calibration matrix. Solid lines represent measured material reflectance, while the dashed curve represents the normalized combined response of the simulated red, green, and near-infrared camera bands.

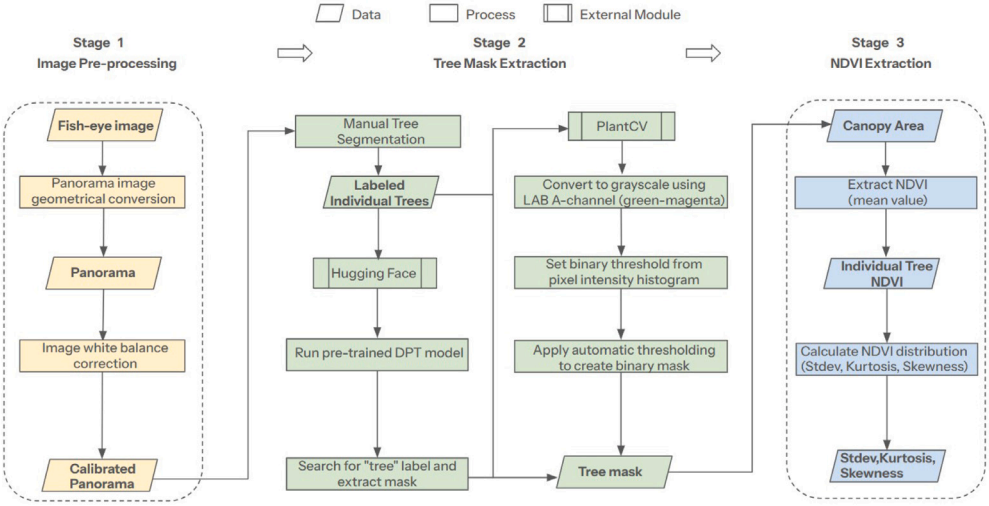

Fig. 5. Image processing pipeline for masking the picture and extracting NDVI values from the segmented and calibrated RAW image.

Table 1
Calibration matrix

Material	Red (%)	Green (%)	NIR (%)
White	91.72	80.31	95.34
Light gray	59.94	51.38	63.31
Dark gray	19.74	18.03	21.25
Black	3.82	4.66	3.93

(iii) to estimate the NDVI value exclusively on tree-related pixels. It is implemented in Python and released open-source on Github.[4]

The pipeline begins with 16-bit uncompressed RAW files containing three channels (RGN). Before any processing occurs, manufacturer-provided sensor response correction is applied.

3.2.1. Stage 1: Image pre-processing

In the first stage, fisheye images are transformed into 360-degree panoramic views by generating a rectilinear representation through geometric transformation. This unwrapping process digitally remaps image pixels into a corrected geometric space and requires the center coordinates and radius of the fisheye projection on the image sensor. These parameters are manually fine-tuned to achieve optimal results (Cai et al., 2022). The output resolution of the panoramic image is a crucial parameter, as it directly affects the processing time of the segmentation algorithms that are applied next. In our case, the resulting, unwrapped, panorama is 4000 × 1380 pixels. The central portion shows the vehicle forward direction, while the left and right quarters display lateral views as shown in Fig. 6.

This transformed panoramic view is compatible with visual AI algorithms and enables effective image segmentation, avoiding the need to apply custom-trained models directly to fisheye views, for which few pre-trained segmentation models are available. Moreover, it improves the interpretability of the images for users. It also demonstrates how a single camera with a fisheye lens can provide a complete 360-degree view of the surrounding environment, making our solution cost-effective.

By design, the calibration target is consistently visible in the outer region of the fisheye image (and the corresponding lower section of the panoramic transformation, see Fig. 6). This setup enables the restoration of each captured image by referencing a calibration matrix derived during preliminary laboratory testing (see Section 3.1.1). In the initial phase, only a single material with a light gray reflectance is used to establish the baseline. The other reference materials serve as indicators to assess potential under- or over-exposure conditions and to verify the overall reliability of the calibration process. The calibration

[4] https://github.com/MIT-Senseable-City-Lab/greenery-scanner.

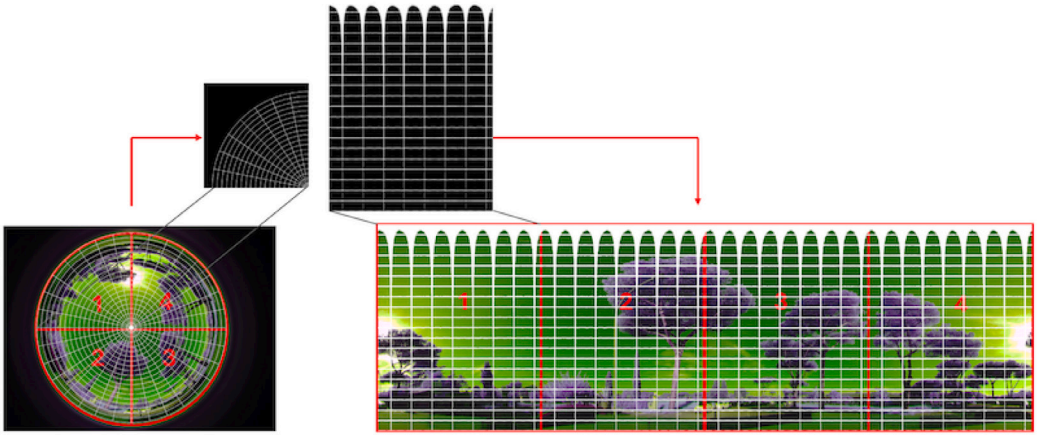

Fig. 6. Fisheye image transformation to 360-panorama view. Image generated using Python (Python Software Foundation, 2023) v3.12.7 and libraries Matplotlib (Matplotlib Development Team, 2025) v3.9.2, OpenCV (OpenCV Team, 2025) v4.10.0, NumPy (NumPy Developers, 2025) v1.26.4, and Numba (Numba Developers, 2025) v0.60.0.

for each image and individual color channel follows the procedure reported in Appendix B.

3.2.2. Stage 2: Tree mask extraction

Segmenting tree canopies in urban environments is challenging due to vegetation diversity, irregular canopy geometry, and highly variable illumination conditions during drive-by data collection. To address these challenges, a two-step approach is adopted to generate tree canopy masks from panoramic views. The segmentation operates on the unwrapped RGN panorama produced in Stage 1 (Section 3.2.1). The same panoramic representation is used both for masking and, subsequently, for NDVI computation. In the first step, semantic segmentation is performed using the Dense Prediction Transformer (DPT) model pre-trained on the ADE20K dataset (Zhou et al., 2017), which provides a robust baseline for distinguishing major urban vegetation categories, including trees and grass. Subsequently, the green channel brightness level is utilized to enhance the distinction between vegetation and non-vegetation regions based on color intensity. A binary threshold is applied to exclude *non-foliage*-related pixels, ensuring that only high-intensity green regions are retained. However, varying illumination conditions across images render fixed thresholds ineffective, often resulting in inaccurate masks, particularly under the inconsistent lighting typical of drive-by data collection. To address this issue, the only data-fitted component of the pipeline is a simple linear model that relates the overall image brightness to a manually validated threshold value. Specifically, for a representative set of panoramic images covering the range of illumination conditions observed during acquisition, the green-channel threshold that best separated foliage from the background was manually identified. A linear regression was then fitted between mean image brightness and the corresponding validated threshold, enabling the optimal threshold to be estimated automatically for unseen images. Pixels with brightness values exceeding the computed threshold are classified as tree regions, while the remaining pixels are assigned to the background. The final binary mask, obtained by combining the DPT-based segmentation with this adaptive refinement, is then applied to the color-corrected image to isolate tree canopies. In cases of extreme illumination artifacts, such as strong backlighting or saturated highlights, segmentation errors may occur. These failure modes can be identified through abnormal brightness distributions and blob-like exposure patterns, allowing rapid identification and optional human supervision during post-processing. Segmentation results under some extreme illumination conditions are presented in Appendix A to illustrate the performance of the system in different urban scenarios. We also manually annotated 84 tree canopies (corresponding to 88 canopy masks, as four trees were captured twice from different directions) used in the field tests, and evaluated the segmentation performance using the Intersection over Union (IoU) and Dice coefficients. To characterize robustness across the different conditions encountered in urban drive-by acquisition, the trees were further grouped into three scene types: single crowns over sky, overlapping crowns over sky, and crowns over built-up backgrounds. Table 2 reports the results. The pipeline achieved an overall mean IoU of 0.862 and a mean Dice of 0.914. Segmentation was most accurate for isolated crowns against sky (IoU 0.900), and slightly lower for overlapping crowns and for crowns against built-up backgrounds (IoU 0.839 and 0.834, respectively). Representative annotated examples across the three scene types are provided in Appendix A (Fig. A.2).

Table 2
Segmentation performance against manually annotated tree crowns.

Scene type	*n*	Mean IoU	Mean Dice
Single crown over sky	33	0.900	0.941
Overlapping crowns over sky	52	0.839	0.896
Crown against building	3	0.834	0.907
Overall	88	0.862	0.914

3.2.3. Stage 3: NDVI extraction

Whereas segmentation is performed on the panoramic RGN representation, NDVI is computed from the calibrated red and NIR channels (Section 3.1.1) and evaluated only on the pixels retained by the tree mask. After generating the tree mask, NDVI values (ranging from −1 to 1) are calculated for each pixel based on the NIR and red reflectance values as follows:

$$\mathrm{NDVI} = \frac{\hat{\mathbf{Im}}_{\mathrm{NIR}} - \hat{\mathbf{Im}}_{\mathrm{red}}}{\hat{\mathbf{Im}}_{\mathrm{NIR}} + \hat{\mathbf{Im}}_{\mathrm{red}}}, \tag{3}$$

where $\hat{\mathbf{Im}}_{\mathrm{NIR}}$ and $\hat{\mathbf{Im}}_{\mathrm{red}}$ represent the channels intensity, respectively. The mean NDVI is computed by averaging the NDVI values of the masked canopy pixels extracted from the imagery.

NDVI values are correlated with leaves chlorophyll content and properties. While the specific range of NDVI values may vary among tree species, higher NDVI values are typically associated with dense and healthy vegetation with robust photosynthetic activity and chlorophyll content, making it a useful proxy for tree health. Conversely, lower values often signal stress from abiotic factors (water or nutrient deficiencies, environmental conditions) or biotic factors (pathogens or parasites) (Bietresato et al., 2016).

4. Results

The GS platform has been evaluated both in a lab setting and on the field. Section 4.1 reports on a controlled laboratory assessment, which was conducted before field deployment to verify that the GS multispectral sensor, custom optical configuration, calibration palette, and image-processing workflow produced stable NDVI estimates on a neutral Spectralon reference target under controlled illumination. This experiment was intended as a functional and radiometric consistency check, not as a comprehensive validation of outdoor measurement accuracy. Section 4.2 then presents the field validation performed in the city of Rome, Italy, where street-level GS-derived NDVI values were compared with arborist-assessed crown dieback in *Pinus Pinea* trees. This analysis addresses the main objective of the study: assessing whether low-cost drive-by multispectral sensing can provide useful indicators of crown dieback severity under real-world urban conditions.

4.1. Validation in lab settings

The validation was carried out using the laboratory setup shown in Fig. 3. The same Spectralon white reference standard used for the characterization of the calibration materials was also acquired with the MAPIR Survey 3 RGN camera mounted on the GS custom fisheye optical configuration. The acquisition was performed using the same image-acquisition modality later adopted in the field deployment. The multispectral LED ring illuminator was kept constant during the whole laboratory session, and its normalized spectral distribution, measured on the Spectralon reference, is reported in Fig. 3(b). This ensured that the validation images were acquired under stable illumination, with radiance contributions over the red and near-infrared wavelength regions used for NDVI estimation. Spectralon was used as a neutral reference target because its reflectance is flat over the red and near-infrared spectral range. Consequently, after calibration, the ratios between the calibrated red, green, and near-infrared channel responses are expected to be close to unity, while the NDVI of the target is expected to be close to zero. These expected values were used as reference targets to quantify the residual error of the calibrated GS pipeline. The calibration and image-processing procedure described in Section 3.2 was applied to the laboratory images using the in-frame calibration palette. For each image, calibration target regions were extracted using fixed polygons corresponding to three repeated positions for each calibration material. A per-channel linear regression was then fitted between the raw camera response and the laboratory-characterized reflectance values across all calibration materials, with three spatial repetitions per material. The validation dataset consisted of 10 laboratory images of the Spectralon reference acquired with the MAPIR camera. For each image, different regions on the Spectralon surface were considered in order to account for possible local illumination gradients, although these were expected to be limited because the target was aligned with the illuminator under controlled laboratory conditions. Within each image, 50 regions were randomly sampled from the Spectralon surface, resulting in 500 bootstrap samples in total. For each sampled region, the calibrated red, green, and near-infrared responses were averaged, and the NIR/R, NIR/G, G/R ratios and NDVI were computed. Residual errors were then calculated with respect to the expected response of a neutral target. Table 3 reports the residual-error statistics of the laboratory validation. The mean values describe the calibrated GS response on the Spectralon target, while bias and RMSE quantify the residual deviations from the expected neutral-target response. The statistics are reported at image level, using the mean response of each laboratory image as an independent observation. This avoids over-interpreting bootstrap samples as fully independent measurements, while still using the bootstrap procedure to account for within-image spatial variability on the Spectralon surface.

The calibrated GS pipeline showed limited residual deviation from the expected neutral response in the red–NIR domain. The mean NIR/R ratio was 1.037, corresponding to a positive bias of 0.037 and an RMSE of 0.037. The residual NDVI error was similarly small, with a mean value of 0.018, a positive bias of 0.018, and an RMSE of 0.018. These results indicate that, under controlled and stable laboratory illumination, the GS acquisition and calibration pipeline preserved the red–NIR consistency required for NDVI estimation within a limited residual error range. The green-related ratios showed larger deviations from unity, particularly for NIR/G and G/R. The NIR/G ratio had a mean value of 1.122, with a positive bias of 0.122 and an RMSE of 0.123. The G/R ratio had a mean value of 0.924, with a negative bias of −0.076 and an RMSE of 0.077. These results indicate that the green channel response was less stable than the red–NIR relationship under the present optical and calibration configuration. This has limited impact on the analyses presented in this work because NDVI is computed only from the red and near-infrared channels. Overall, this laboratory validation should be interpreted as a functional and radiometric consistency check of the GS sensor and image-processing pipeline before outdoor deployment. It verifies that the camera, custom optical configuration, calibration palette, and image-processing workflow operate coherently under controlled laboratory illumination. Outdoor acquisitions remain more complex because they are affected by changing illumination, canopy self-shadowing, lens vignetting, partial occlusions, viewing perspective, and segmentation uncertainty. These factors are therefore addressed as limitations of the present study and as priorities for future controlled experiments in Section 5.

Table 3
Laboratory residual-error assessment of the calibrated GS pipeline on a Spectralon reference standard.

Metric	Ideal	Mean	Std	Bias	RMSE
NIR/R	1.0	1.037	0.006	+0.037	0.037
NIR/G	1.0	1.122	0.010	+0.122	0.123
G/R	1.0	0.924	0.011	−0.076	0.077
NDVI	0.0	0.018	0.003	+0.018	0.018

4.2. Validation in real-world setting

In-situ data collection was conducted in the city of Rome, Italy, to evaluate the GS platform under real-world urban conditions. Three main sources of information were collected in the study area: (i) visual inspection performed by licensed arborists, (ii) street-level NDVI measurements obtained using GS, and (iii) aerial NDVI measurements using a drone equipped with a multispectral camera. To maintain focus on the primary contribution of this work, only the GS-based analysis with respect to arborists inspections is reported in this Section, while drone-derived results are presented as contextual evidence in Section 5. The study area was selected based on two main criteria. First, the area is characterized by a dominant tree species (*Pinus pinea*), which reduces inter-species variability in NDVI measurements, as different species are known to exhibit distinct spectral reference ranges (Acosta-Hernández et al., 2024). Second, a substantial number of trees in the area exhibited visible crown dieback, a parasitic condition that primarily affects the lower portions of the canopy and progressively compromises overall tree health (Marchin et al., 2022). In the selected area, crown dieback was mainly associated with infestation by the parasite *Toumeyella parvicornis*. Licensed arborists inspections were carried out during early September 2024, while GS and drone data collection occurred during early October 2024. It is important to note that arborists assessments provide expert qualitative evaluations based on visual and structural inspection rather than direct spectral measurements. Accordingly, their assessments are used in this study as a contextual reference for interpreting GS-derived NDVI values, rather than as a spectral ground-truth benchmark.

One GS was deployed on a vehicle driving at approximately 25 km/h along a predefined route over the study area, collecting

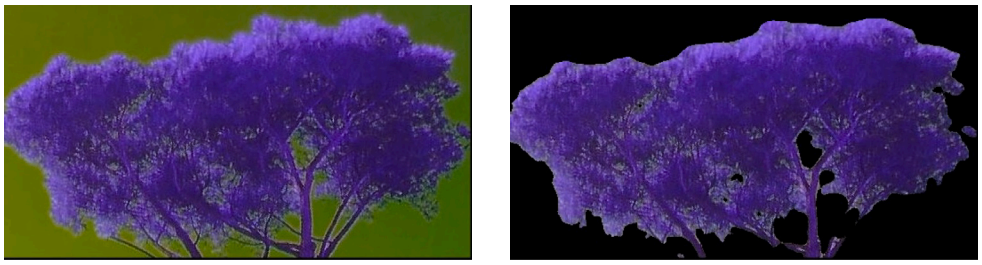

(a) (b)

Fig. 7. (a) Manually identified tree crown for the tree with the *id* = 42. **(b)** Tree mask after the segmentation algorithm applied (see Section 3.2.2).

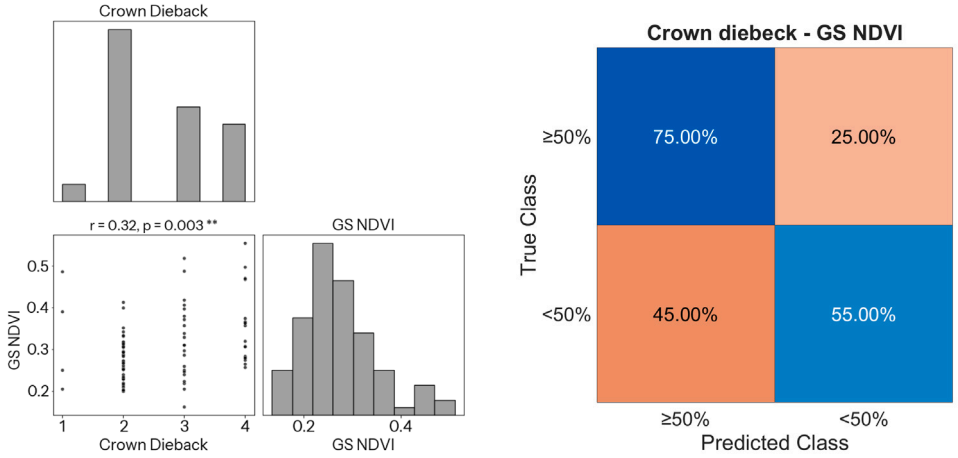

(a) (b)

Fig. 8. (a) Linear correlation between GS-measured NDVI and crown dieback. Crown dieback have been manually assessed by experts in 4 levels: 0%–25% (1) 25%–50% (2) 50%–75% (3) and 75%–100% (4). (b) Logistic regression results classifying trees highly affected by crown dieback (≥50%) and slightly affected by crown dieback (<50%).

multispectral images every 5 s. After data collection, 325 images that contained greenery were retained, and greenery masks were extracted by applying the image processing pipeline described in Section 3.2.2. Segmentation performance across four representative illumination conditions encountered during the field deployment is reported in Appendix A (Fig. A.1), illustrating both the robustness of the pipeline under favorable conditions and its failure modes under direct sunlight and backlighting. It has to be noted that the masked portion of each image may contain crowns belonging to one or more trees, as the GS AI pipeline can only extract NDVI values by averaging all the tree crowns visible in the camera field of view, without being able to identify single tree instances. Instead of extracting NDVI values from the whole masked greenery, for evaluation purposes, tree crowns represented in GS images were matched with arborist crown dieback assessments, adopting a two-stage procedure. First, tree instances were preliminarily associated based on spatial proximity using GPS coordinates. Subsequently, each match was manually verified, and the corresponding crown regions were cropped to guarantee alignment between the GS multispectral imagery and the annotations from the arborists. Finally NDVI values for each tree have been computed by averaging masked canopy pixels obtained through the proposed segmentation pipeline (see Fig. 7). This procedure yielded a final dataset of 84 unique trees for which both NDVI values collected by GS and crown dieback assessments from arborists existed.

To investigate the relationship between crown dieback severity assessed by arborists and the mean NDVI values estimated by the GS a linear regression model was fitted using the mean NDVI as the dependent variable and crown dieback classes as the independent variable. According to the arborist assessments, 18 trees exhibited crown dieback <25%, 22 between 25%–50%, 40 between 50%–75%, and 4 > 75%. The results reported in Fig. 8(a), indicate a statistically significant association between NDVI and crown dieback severity ($p < 0.01$).

Moreover an observable trend emerges in which trees with lower crown dieback levels exhibit higher NDVI values, whereas increasing dieback severity corresponds to lower NDVI measurements. This behavior is consistent with the expected spectral response, as canopy thinning and foliage loss reduce the near-infrared reflectance captured by the GS platform. Although the correlation strength is moderate, the statistically significant result confirms that GS-derived NDVI is sensitive to variations in canopy condition observable from street level. The correlation is also illustrated in Fig. 9, where the outer circle represents the GS-derived NDVI value and the inner point indicates the crown dieback level assessed by arborists. Distinct spatial patterns can be observed, with clusters of trees affected by the parasite consistently reflected in lower GS-based NDVI values.

While linear regression quantifies the strength and direction of the association between NDVI and crown dieback severity, a classification approach improves interpretability by translating NDVI measurements into defined severity categories.

Given the limited sample size ($n = 84$) and the imbalance among the four dieback classes (particularly the small number of trees with dieback >75%), a binary classification framework was adopted to improve statistical robustness. The four classes were therefore aggregated into two categories:

- Early/low dieback: <50%

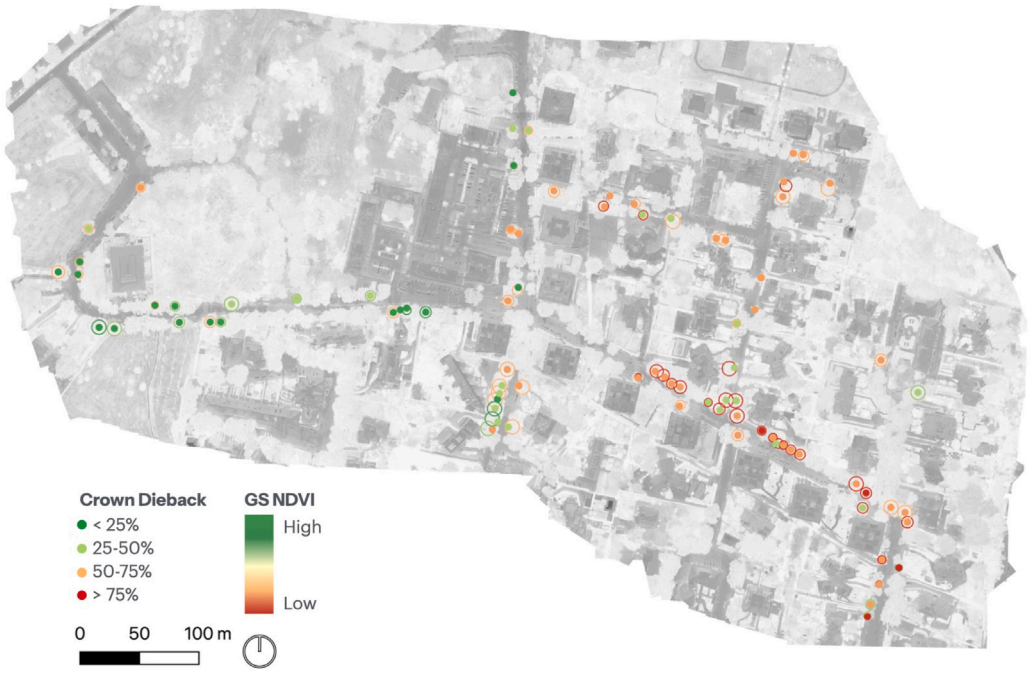

Fig. 9. Spatial distribution of trees along Via Marcello Garosi, Rome, Italy (41°47′53.6″N, 12°26′58.4″E), illustrating the relationship between arborist-assessed crown dieback severity and GS-derived street-level NDVI measurements. Each tree is represented by a circular marker, where the inner filled circle denotes crown dieback severity assessed by licensed arborists and categorized into four classes (<25%, 25%–50%, 50%–75%, and >75%), while the outer ring encodes the corresponding NDVI value measured by the GS platform using a continuous color scale. The background map is displayed in grayscale to provide spatial context while emphasizing tree-level information. The base map was generated from aerial imagery using Pix4DField v2.7.2 (Pix4D S.A., 2025) and annotated using QGIS v3.38.3 (QGIS Development Team, 2024). (For interpretation of the references to color in this figure legend, the reader is referred to the web version of this article.)

- Severe dieback: ≥50%

A binary logistic regression model was trained using GS-derived mean NDVI as predictor. Model validation was performed using 5-fold cross-validation to ensure greater statistical robustness and to mitigate overfitting effects given the small dataset size. The overall classification accuracy obtained across folds was 66%. The corresponding confusion matrix is reported in Fig. 8(b). The confusion matrix reveals a tendency toward false positives (trees predicted as having severe crown dieback (≥50%) that were in fact classified as <50% by arborists. This behavior suggests that GS-derived NDVI may be particularly sensitive to early/low canopy stress signals, potentially identifying reductions in vegetation vigor before they are visually assessed as severe dieback by arborist inspections. Despite this bias, the model demonstrates a reasonable discrimination capability considering the simplicity of the predictor (single mean NDVI value) and the limited dataset size.

5. Discussion

This section discusses the main findings of the study, interpreting the results in relation to drone- and satellite-based approaches in order to highlight the role of sensing perspective, operational applicability, current workflow limitations; and defining future research directions.

The association between GS-derived NDVI and arborist-assessed crown dieback supports the interpretation that red–NIR vegetation indices can capture canopy-condition signals relevant to urban tree health. Prior work on *T. parvicornis* infestation in *Pinus pinea* in Rome used PlanetScope satellite time series and the Renormalized Difference Vegetation Index (RDVI), an NDVI-derived red-NIR index, to discriminate healthy and unhelty trees (Falanga et al., 2024). Other airborne studies have related vegetation indices to field-assessed crown condition, although the specific indices and target variables differ. For example, Evans et al. (2012) find that NDVI and REEI (Red-Edge Extrema Index) indexes are suitable for crown diebeck detection. Similarly, Morales-Gallegos et al. (2023) evaluated NDVI and BNDVI (blue-NDVI) finding that both indicators are associated with crown-density and crown-transparency. These studies therefore provide evidence that red–NIR vegetation indices, including but not limited to NDVI, are sensitive to canopy-condition signals from a top-down perspective. The 66% binary classification accuracy obtained by GS should be interpreted under its specific acquisition constraints: a single mean NDVI predictor, a tree-level dataset of 84 *Pinus pinea* trees, street-level drive-by perspective, and uncontrolled outdoor illumination. This setting differs from satellite time-series analyses and planned airborne acquisitions, and is consistent with the intended role of GS as a first-pass screening tool for prioritizing trees that require follow-up inspection rather than as a stand-alone diagnostic classifier. Beyond classification performance, GS offers practical advantages over aerial and satellite alternatives in terms of cost, operational flexibility, and revisit frequency. Satellite-based monitoring platforms such as PlanetScope involve subscription costs that are typically prohibitive for municipal-scale deployments, and revisit times are constrained by orbital periods and cloud cover (Falanga et al., 2024). UAV surveys require flight planning, regulatory clearance, and skilled operators, limiting their use to periodic campaigns (Näsi et al., 2018). In contrast, GS can be deployed on existing vehicle fleets (taxis, delivery vans, municipal maintenance vehicles) at a sub-1000 USD cost per unit, enabling daily or weekly revisits along urban road corridors without limitations typical of airborne operations. This revisit frequency is particularly valuable for monitoring fast-evolving stress conditions such as pest outbreaks (such as Toumeyella parvicornis outbreaks), where early detection within a single season can meaningfully inform management decisions. Importantly, GS is not conceived as a replacement for aerial or satellite observations but as a complementary layer. As demonstrated with our findings, GS-derived NDVI was significantly associated with arborist-assessed crown dieback, and the subsequent comparison with drone-derived NDVI further supports

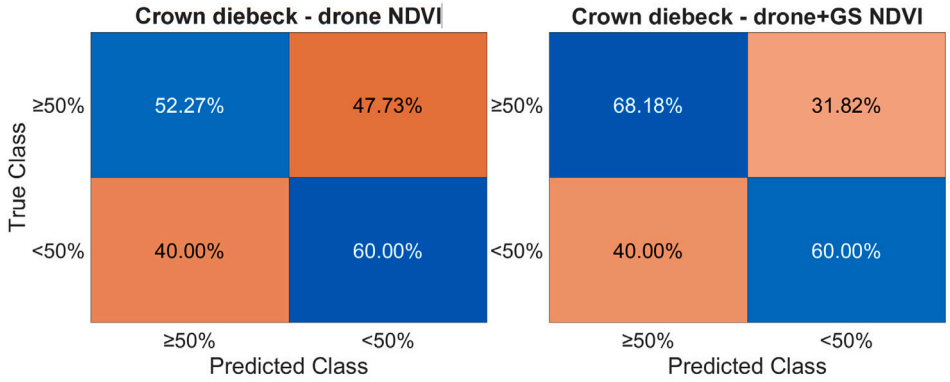

Fig. 10. Binary logistic regression performance using (left) drone-derived mean NDVI and (right) combined drone and GS mean NDVI as predictors. Trees are grouped into two classes: low/early crown dieback (<50%) and severe crown dieback (≥50%). Values are row-normalized percentages aggregated across 5-fold cross-validation.

the interpretation that street-level and top-down acquisitions capture complementary canopy-condition information. These perspectives can therefore be fused to provide a more complete picture of urban tree condition across spatial scales This complementarity is not only operational, but also related to the sensing perspective. Crown dieback in *Pinus pinea* is frequently observed to initiate and progress in the lower and inner portions of the canopy (Marchin et al., 2022). These regions are directly visible from the street but can be partially occluded from aerial views. As a result, GS measurements are more likely to reflect stress signals linked to foliage loss and reduced photosynthetic activity when dieback is at an early stage, while aerial NDVI (e.g. via drones or satellites) is more sensitive to severe dieback.

To assess whether GS provides complementary information with respect to top-down multispectral sensing, we compared street-level GS-derived NDVI with drone-derived NDVI on the same binary crown-dieback classification task. Specifically, both sensing modalities were evaluated on the same set of *Pinus pinea* trees using the same binary formulation, low/early crown dieback (<50%) versus severe crown dieback (≥50%), and the same 5-fold cross-validation protocol. Under the same binary formulation (<50% vs. ≥50% dieback) and the same validation protocol, the logistic regression model based on drone NDVI alone shows reduced performance (overall accuracy of 56%) compared to GS, particularly in terms of classification for the ≥50% class (Fig. 10(left)). This suggests that top-down NDVI measurements may be less sensitive to dieback when the upper canopy remains comparatively intact. Combining drone and GS NDVI (Fig. 10(right)) yields a performance comparable to GS alone (overall accuracy of 64%) yet shifting the error profile: false positives are reduced, but at the cost of more false negatives. This result suggests that aerial and street-level NDVI capture complementary but not redundant information.

From an operational standpoint, the GS platform is conceived as a first-pass screening layer rather than a complete diagnostic tool, and its performance profile should be evaluated accordingly. In a scenario where arborist inspections are a limited resource that must be prioritized across a large urban area, a drive-by NDVI survey can identify candidate trees exhibiting low spectral vitality, enabling inspection efforts to be concentrated on a smaller, higher-risk subset (Gupta et al., 2024a; Koeser et al., 2017). In this context, the tendency of the GS classifier toward false positives, predicting severe dieback in trees subsequently assessed as <50% by arborists (Fig. 8(b)), may be operationally acceptable: triggering an unnecessary inspection is less consequential than missing a severely declining tree. Furthermore, as the platform is deployed on vehicles that routinely traverse the same corridors, repeated observations over multiple passes can be aggregated to increase the robustness of NDVI estimates by reducing the influence of image-specific errors caused by direct sunlight, backlighting or localized overexposure, which are illustrated in Fig. A.1, thereby improving screening reliability over time.

Despite these promising results, several limitations remain. First, NDVI estimation is still sensitive to illumination variability, particularly under strong backlighting or localized overexposure, conditions that are mainly observed on sunny days. In addition, canopy self-shadowing may attenuate NIR reflectance independently of tree health, while complex urban scenes can introduce residual segmentation errors due to building occlusions, overlapping crowns or densely layered vegetation. These factors can bias the NDVI values extracted from masked canopy pixels and should be explicitly considered when interpreting GS measurements. Future work will investigate improved radiometric calibration strategies that incorporate solar position, urban 3D shading models, weather data, and onboard light sensing to enable dynamic adjustment.

Second, segmentation accuracy may decrease in complex urban scenarios involving overlapping or densely layered canopies. This is consistent with the segmentation quality assessment (Table 2), where accuracy was highest for isolated crowns against sky and lower for overlapping crowns and built-up backgrounds, which offer less contrast between the target canopy and its surroundings. Moreover, the current workflow remains canopy-level rather than fully tree-instance-based. The segmentation pipeline extracts vegetation masks from panoramic images, but a single masked region may include crowns from multiple adjacent trees. In this study, GS-derived canopy NDVI was associated with individual arborist-assessed trees through GPS-based matching followed by manual verification, as described in Section 4.2. While suitable for this validation dataset, this semi-manual procedure limits scalability for repeated large-area deployments. Developing custom-trained segmentation models tailored to street-level vegetation scenes is expected to improve crown delineation and reduce bias in NDVI estimation. Future work should also address automated single-tree instance segmentation, georeferenced tree matching, and temporal tracking across repeated drive-by acquisitions.

Future iterations of GS will explore edge-oriented implementations. By adopting lightweight, task-specific models and optimized inference pipelines, vegetation-related features could be extracted directly on-device, thereby reducing data transmission requirements, lowering operational costs, and facilitating compliance with privacy-preserving regulations by minimizing raw image storage and transfer.

Third, the validation was limited to a single dominant species, *Pinus pinea*, at one urban site in Rome, where crown dieback was primarily associated with *Toumeyella parvicornis*. This design choice reduced inter-species spectral variability and allowed the analysis to focus on the target disease process; however, it also constrains the direct generalization of the findings to mixed-species urban forests. Because NDVI reference ranges, crown architecture, and stress responses vary across species and sites, future deployments should include multi-species and multi-site datasets. Integrating AI-based species identification could

further enable species-aware NDVI baselines and more robust per-species screening thresholds.

Finally, multi-source data fusion represents a promising direction for future research. Integrating GS street-level observations with UAV imagery and satellite time series may improve sensitivity to different canopy layers, enhance temporal coverage, and increase robustness. Multi-view or hierarchical learning frameworks could combine fine-grained street-level information with broader top-down context, enabling more accurate, scalable, and operational urban tree health monitoring across seasons, species, and geographic contexts.

6. Conclusion

Urban forests provide multiple ecosystem services, yet urban trees are increasingly exposed to biotic and abiotic stressors that require frequent and scalable monitoring. Traditional visual inspections by arborists remain reliable but are labor-intensive and thus spatially sparse. Remote sensing approaches based on UAVs or satellites provide broader spatial coverage; however, they face operational constraints (e.g., regulatory restrictions, costs) and limited sensitivity to lower-canopy conditions, which often contain early signals of biotic stressors.

To complement existing methods, the Greenery Scanner (GS) platform was developed as an open-source, low-cost, drive-by solution for street-level vegetation monitoring. The system integrates environmental sensors with a multispectral fisheye camera for NDVI estimation and is supported by a visual AI pipeline that: (i) unwraps RGN fisheye imagery into panoramic views, (ii) performs color correction, (iii) extracts tree canopy masks, and (iv) computes NDVI aggregated over the masked regions. Rather than replacing established inventory or diagnostic approaches, GS is conceived as a complementary screening tool capable of providing bottom-up canopy-level insights along urban mobility corridors. These insights can support the prioritization of arborist inspections and UAV surveys.

Laboratory validation under controlled illumination demonstrated that GS-derived NDVI values are consistent with measurements from a reference hyperspectral system. In a real-world deployment in Rome, street-level GS NDVI showed a statistically significant association with arborist-assessed crown dieback severity in *Pinus pinea*. When formulated as a binary classification task (<50% vs. ≥50% dieback), a logistic regression model based on mean GS NDVI achieved a cross-validated accuracy of 66%. These findings support the feasibility of street-level multispectral sensing as a scalable screening layer for identifying decline patterns, particularly those affecting lower canopy portions that are less detectable through top-down UAV or satellite observations.

We envision GS as a research platform for investigating the relationships between urban greenery health and spectral response across diverse urban contexts. To this end, the platform's open-source license and modular design enable the integration of additional imaging sensors (e.g., thermal cameras) and adaptation to multiple deployment configurations. We also aim to support integration with citizen-science approaches, enabling communities to fabricate GSs using off-the-shelf components and consumer-grade 3D printers, and to deploy them on private vehicles. In this model, communities work in tandem with researchers and practitioners to collect and analyze data. Such distributed deployments can substantially increase spatial coverage while fostering local engagement in urban environmental monitoring. Finally, arborists and urban forest managers could use GS as a cost-effective screening tool to help prioritize inspections over large areas, identify early signs of vegetation stress, and optimize maintenance interventions.

CRediT authorship contribution statement

Leonardo Iacussi: Writing – review & editing, Writing – original draft, Software, Methodology, Investigation, Formal analysis, Data curation. **Song Guo:** Writing – review & editing, Writing – original draft, Software, Methodology, Investigation, Formal analysis, Data curation. **Simone Mora:** Writing – review & editing, Writing – original draft, Validation, Supervision, Project administration, Methodology, Investigation, Funding acquisition, Formal analysis, Data curation, Conceptualization. **Andrei Speridĭao:** Visualization, Software, Methodology, Investigation. **Oluwatobi Oyinlola:** Validation, Software, Data curation. **Giancarlo Papitto:** Validation, Supervision, Resources, Funding acquisition, Conceptualization. **Umberto Fugiglando:** Methodology, Funding acquisition, Conceptualization. **Paolo Chiariotti:** Supervision. **Alfredo Cigada:** Supervision. **Carlo Ratti:** Supervision, Funding acquisition.

Declaration of competing interest

The authors declare that they have no known competing financial interests or personal relationships that could have appeared to influence the work reported in this paper.

Acknowledgments

The authors would like to thank the financial support received from the members of the Senseable City Lab consortium, including Consiglio per la Ricerca in Agricoltura e l'Analisi dell'Economia Agraria, the AMS Institute, Dubai Future Foundation, Arnold Ventures, Toyota, UnipolTech, Toyota Woven City, Tele2, Volkswagen Group America, FAE Technology, Fédération Internationale de l'Automobile, Amsterdam and Rio de Janeiro. We'd like to thank CUFAA "Comando unità forestali, ambientali e agroalimentari" for providing support during data collection in the City of Rome and to Sanjana Ryali for her contribution on data validation and analysis.

Appendix A. Segmentation results and examples

In Fig. A.1, the left panels show false-color multispectral panoramic images, while the right panels display the corresponding binary tree masks obtained through the proposed two-step segmentation pipeline. Under relatively uniform or diffuse illumination conditions, tree canopies are consistently and accurately delineated. In more challenging cases involving strong backlighting or localized overexposure, partial segmentation errors may occur, such as canopy thinning or sky intrusion. These failure modes are characteristic of drive-by street-level imaging and are explicitly accounted for in the pipeline through adaptive thresholding and image-level supervision. Additional examples illustrate that, despite illumination variability, the proposed approach remains effective for isolating canopy-level vegetation signals across a wide range of real-world urban environments.

Fig. A.2 shows representative results from the segmentation performance evaluation (Table 2) across the three scene types. For each example, the manual annotation and the pipeline output are overlaid on the original crop, showing regions of agreement together with annotation-only and prediction-only regions.

Appendix B. Target calibration procedure

The subsequent formulation reports the calibration formula used to calibrate the multispectral camera channels. It is reported only for red channels but then is applied also to NIR and Green channels.

$$\hat{\mathbf{Im}}_{\mathrm{red}}(x,y) = \mathbf{Im}_{\mathrm{red}}(x,y) \times \left(\frac{\mathrm{Red}[\%]_{\mathrm{lg}}}{\bar{\mathbf{Im}}_{\mathrm{red}}(x_{\mathrm{lg}}, y_{\mathrm{lg}})} \times \frac{65536}{100} \right), \tag{B.1}$$

where $\hat{\mathbf{Im}}_{\mathrm{red}}$ is the red channel of the calibrated image, $\mathbf{Im}_{\mathrm{red}}$ is the red channel of the original image, $\mathrm{Red}[\%]_{\mathrm{lg}}$ is the reflectance value of the light gray material extracted from Table 1, and $\bar{\mathbf{Im}}_{\mathrm{red}}(x_{\mathrm{lg}}, y_{\mathrm{lg}})$ corresponds to the average pixel value in the light gray region of the original image. 65 536 and 100 are the normalization terms for, respectively, the 16-bit range of each pixel and the percentage normalization of the reflectance. This same normalization procedure can be applied to the other two channels or with different calibration materials. This approach serves as a valuable verification check.

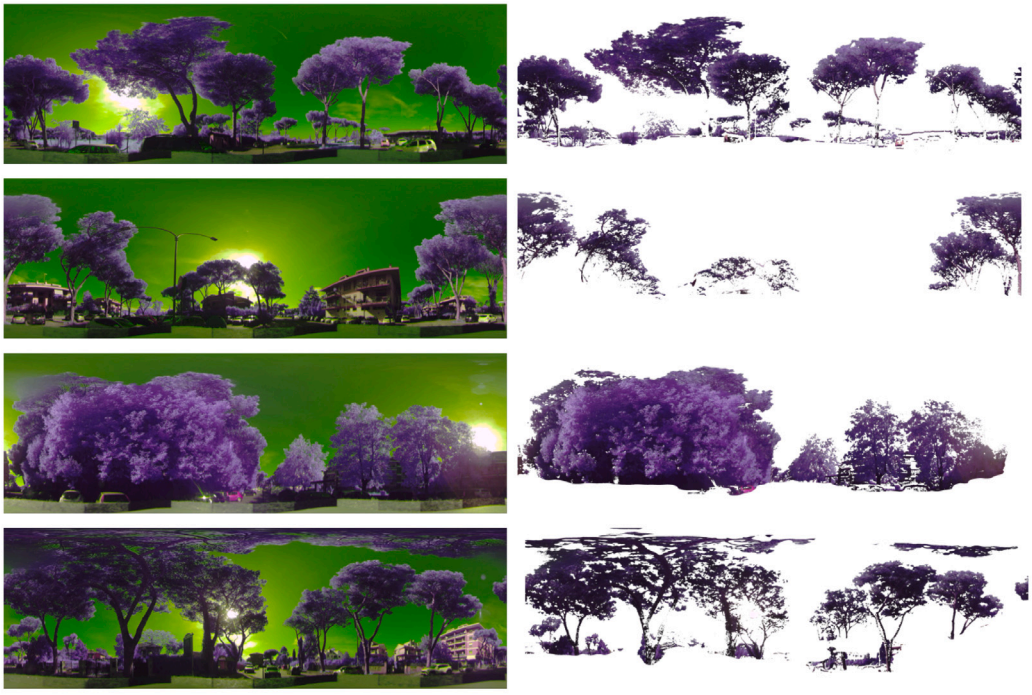

Fig. A.1. Tree canopy segmentation results under four representative illumination conditions encountered during drive-by data collection. Left panels show false-color RGN panoramic images; right panels show the corresponding binary tree masks produced by the two-step segmentation pipeline (Section 3.2.2). (For interpretation of the references to color in this figure legend, the reader is referred to the web version of this article.)

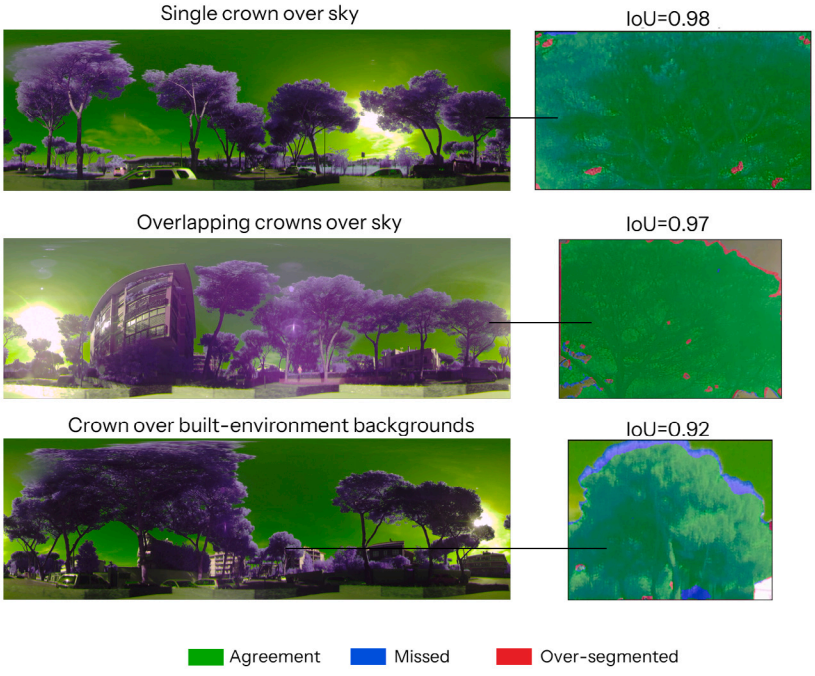

Fig. A.2. Representative tree-crown segmentation results for the three scene types.

References

Acosta-Hernández, A.C., Pompa-García, M., Martínez-Rivas, J.A., Vivar-Vivar, E.D., 2024. Cutting the greenness index into 12 monthly slices: How Intra-Annual NDVI dynamics help decipher drought responses in mixed forest tree species. Remote. Sens. 16 (2), 389. http://dx.doi.org/10.3390/rs16020389.

Anjomshoaa, A., Duarte, F., Rennings, D., Matarazzo, T.J., deSouza, P., Ratti, C., 2018. City scanner: Building and scheduling a mobile sensing platform for smart city services. IEEE Internet Things J. 5 (6), 4567–4579. http://dx.doi.org/10.1109/JIOT.2018.2839058.

Bahe, M.M., Murphy, R.L., Russell, M.B., Knight, J.F., Johnson, G.R., 2021. Suitability of a single imager multispectral sensor for tree health analysis. Urban For. Urban Green. 63, 127187. http://dx.doi.org/10.1016/j.ufug.2021.127187, URL https://www.sciencedirect.com/science/article/pii/S1618866721002120.

Baldocchi, D., Chu, H., Reichstein, M., 2018. Inter-annual variability of net and gross ecosystem carbon fluxes: A review. Agricult. Forest. Meterol. 249, 520–533. http://dx.doi.org/10.1016/j.agrformet.2017.05.015.

Balios, V.A., Ortega, S., Heia, K., Avetisyan, A., Krause, K., 2026. Assisting species differentiation and taxonomic classification by hyperspectral imaging: an example from the parasitic plant realm. Plant Methods http://dx.doi.org/10.1186/s13007-025-01498-y.

Bietresato, M., Carabin, G., D'Auria, D., Gallo, R., Ristorto, G., Mazzetto, F., Vidoni, R., Gasparetto, L., 2016. A tracked mobile robotic lab for monitoring the plants volume and health. In: 2016 12th IEEE/ASME International Conference on Mechatronic and Embedded Systems and Applications (MESA). http://dx.doi.org/10.1109/MESA.2016.7587134.

Cai, J., Yang, K., Cheng, L., Wang, Y., 2022. Pixel-Wise fisheye image correction method with Single-View phase target. IEEE Photonics Technol. Lett. 34 (19), 1038–1041. http://dx.doi.org/10.1109/LPT.2022.3199616.

Cavender-Bares, J., Nelson, E., Meireles, J., Lasky, J., MIteva, D., Nowak, D., 2022. The hidden value of trees: Quantifying the ecosystem services of tree lineages and their major threats across the contiguous US. PLOS Sustain. Transform. 1 (4), http://dx.doi.org/10.32942/osf.io/gp7mt.

CEVA-IP, 2025. BNO085/BNO086 9-Axis System-in-Package. URL https://www.ceva-ip.com/product/bno-9-axis-imu/.

Chi, D., Degerickx, J., Yu, K., Somers, B., 2020. Urban tree health classification across tree species by combining airborne laser scanning and imaging spectroscopy. Remote. Sens. 12 (15), http://dx.doi.org/10.3390/rs12152435, URL https://www.mdpi.com/2072-4292/12/15/2435.

Cruz-Guerrero, I.A., Leon, R., Granados-Castro, L., Fabelo, H., Ortega, S., Campos-Delgado, D.U., Callico, G.M., 2022. Reflectance calibration with normalization correction in hyperspectral imaging. In: 2022 25th Euromicro Conference on Digital System Design. DSD, pp. 855–862. http://dx.doi.org/10.1109/DSD57027.2022.00120.

Dash, J.P., Pearse, G.D., Watt, M.S., 2018. UAV multispectral imagery can complement satellite data for monitoring forest health. Remote. Sens. 10 (8), http://dx.doi.org/10.3390/rs10081216, URL https://www.mdpi.com/2072-4292/10/8/1216.

Dowtin, A.L., Cregg, B.C., Nowak, D.J., Levia, D.F., 2023. Towards optimized runoff reduction by urban tree cover: A review of key physical tree traits, site conditions, and management strategies. Landsc. Urban Plan. 239, 104849. http://dx.doi.org/10.1016/j.landurbplan.2023.104849.

Evans, B., Lyons, T.J., Barber, P.A., Stone, C., Hardy, G., 2012. Dieback classification modelling using high-resolution digital multispectral imagery and in situassessments of crown condition. Remote. Sens. Lett. 3 (6), 541–550. http://dx.doi.org/10.1080/01431161.2011.639400.

Falanga, V., Francini, S., Parisi, F., Cavalli, A., De Fioravante, P., Cucca, B., D'Amico, G., Chirici, G., Lasserre, B., Ottaviano, M., Munafò, M., Marchetti, M., 2024. Near-Real-Time detection of insect outbreaks in Urban trees using a PlanetScope time series. Forests 15 (12), 2261. http://dx.doi.org/10.3390/f15122261.

Faqeerzada, M.A., Kim, H., Kim, M.S., Baek, I., Chan, D.E., Cho, B.-K., 2025. Hyperspectral imaging VIS-NIR and SWIR fusion for improved drought-stress identification of strawberry plants. Comput. Electron. Agric. 237, 110702. http://dx.doi.org/10.1016/j.compag.2025.110702.

Fernandez-Figueroa, E.G., Wilson, A.E., Rogers, S.R., 2021. Commercially available unoccupied aerial systems for monitoring harmful algal blooms: A comparative study. Limnol. Ocean.: Methods 20 (3), 146–158. http://dx.doi.org/10.1002/lom3.10477.

Fuentes, S., Tongson, E., Gonzalez Viejo, C., 2021. Urban green infrastructure monitoring using remote sensing from integrated visible and thermal infrared cameras mounted on a moving vehicle. Sensors 21 (1), 295.

Genesi Elettronica, 2025. Multispectral lighting system. URL https://www.genesi-elettronica.com/it/product/multispectral-lighting/.

Gomes, A.P.A., Queiroz, D.M.d., Valente, D.S.M., Pinto, F.d.A.d.C., Rosas, J.T.F., 2021. Comparing a single-sensor camera with a multisensor camera for monitoring coffee crop using unmanned aerial vehicles. Eng. Agric. 41 (1), 87–97. http://dx.doi.org/10.1590/1809-4430-eng.agric.v41n1p87-97/2021.

Gupta, A., Mora, S., Preisler, Y., Duarte, F., Prasad, V., Ratti, C., 2024a. Tools and methods for monitoring the health of the urban greenery. Nat. Sustain. 7 (5), 536–544. http://dx.doi.org/10.1038/s41893-024-01295-w.

Gupta, A., Mora, S., Zhang, F., Rutten, M., Venkatesha Prasad, R., Ratti, C., 2024b. GreenScan: Toward large-scale terrestrial monitoring the health of urban trees using mobile sensing. IEEE Sens. J. 24 (13), 21286–21299. http://dx.doi.org/10.1109/JSEN.2024.3397490.

Hanh, B.T., Manh, H.V., Nguyen, N.-V., 2022. Enhancing the performance of transferred efficientnet models in leaf image-based plant disease classification. J. Plant Dis. Prot. 129 (4), 623–634. http://dx.doi.org/10.1007/s41348-022-00601-y, URL https://link.springer.com/article/10.1007/s41348-022-00601-y.

Kagan, D., Fuhrmann Alpert, G., Fire, M., 2021. Automatic large scale detection of red palm weevil infestation using street view images. ISPRS J. Photogramm. Remote Sens. 182, 122–133. http://dx.doi.org/10.1016/j.isprsjprs.2021.10.004.

Khan, A., Asim, W., Ulhaq, A., Ghazi, B., Robinson, R.W., 2021. Health assessment of eucalyptus trees using siamese network from Google street and ground truth images. Remote. Sens. 13 (11), 2194. http://dx.doi.org/10.3390/rs13112194.

Knipling, E.B., 1970. Physical and physiological basis for the reflectance of visible and near-infrared radiation from vegetation. Remote Sens. Environ. 1 (3), 155–159. http://dx.doi.org/10.1016/s0034-4257(70)80021-9.

Koeser, A.K., Hauer, R.J., Klein, R.W., Miesbauer, J.W., 2017. Assessment of likelihood of failure using limited visual, basic, and advanced assessment techniques. Urban For. Urban Green. 24, 71–79. http://dx.doi.org/10.1016/j.ufug.2017.03.024.

Labsphere, Inc, 2024. Spectralon reflectance material. https://www.labsphere.com.

Lausch, A., Erasmi, S., King, D.J., Magdon, P., Heurich, M., 2016. Understanding forest health with remote sensing -Part I—A review of spectral traits, processes and remote-sensing characteristics. Remote. Sens. 8 (12), http://dx.doi.org/10.3390/rs8121029, URL https://www.mdpi.com/2072-4292/8/12/1029.

Li, X., Zhang, C., Li, W., Ricard, R., Meng, Q., Zhang, W., 2015. Assessing street-level urban greenery using Google Street View and a modified green view index. Urban For. Urban Green. 14 (3), 675–685. http://dx.doi.org/10.1016/j.ufug.2015.06.006.

Liu, D., Lv, F., Guo, J., Zhang, H., Zhu, L., 2023. Detection of forestry pests based on improved YOLOv5 and transfer learning. Forests 14 (7), http://dx.doi.org/10.3390/f14071484, URL https://www.mdpi.com/1999-4907/14/7/1484.

Lozoya, C., Eyzaguirre, E., Espinoza, J., Montes-Fonseca, S.L., Rosas-Perez, G., 2019. Spectral vegetation index sensor evaluation for greenhouse precision agriculture. In: 2019 IEEE SENSORS. pp. 1–4. http://dx.doi.org/10.1109/SENSORS43011.2019.8956911.

Lu, S., Bao, S., Shi, W., Wei, Y., Zhang, S., Yang, D., 2025. Multimodal sensor dataset from vehicle-mounted mobile mapping system for comprehensive urban scenes. Sci. Data 12 (1), http://dx.doi.org/10.1038/s41597-025-05471-1.

MAPIR, 2025a. Advanced V2 GNSS receiver. URL https://www.mapir.camera/collections/survey-camera-accessories/products/survey3-advanced-v2-gps-receiver.

MAPIR, 2025b. OCN filter improves results compared to RGN filter. URL https://www.mapir.camera/en-gb/pages/ocn-filter-improves-contrast-compared-to-rgn-filter.

Marchin, R.M., Esperon-Rodriguez, M., Tjoelker, M.G., Ellsworth, D.S., 2022. Crown dieback and mortality of urban trees linked to heatwaves during extreme drought. Sci. Total Environ. 850, 157915. http://dx.doi.org/10.1016/j.scitotenv.2022.157915.

Matplotlib Development Team, 2025. Matplotlib: Visualization with Python. URL https://matplotlib.org.

Merdymshaeva, E., Mora, S., Machida, Y., Zhang, F., Duarte, F., Paul, S., Ratti, C., Mörtberg, U., 2025. Assessing the impact of greenery on urban heat using opportunistic drive-by sensing. Environ. Plan. B 23998083241311068. http://dx.doi.org/10.1177/23998083241311068.

Mora, S., Anjomshoaa, A., Benson, T., Duarte, F., Ratti, C., 2019. Towards Large-scale Drive-by Sensing with Multi-purpose city scanner nodes. In: 2019 IEEE 5th World Forum on Internet of Things. WF-IoT, pp. 743–748. http://dx.doi.org/10.1109/WF-IoT.2019.8767186.

Morales-Gallegos, L.M., Martínez-Trinidad, T., Hernández-de la Rosa, P., Gómez-Guerrero, A., Alvarado-Rosales, D., Saavedra-Romero, L.d., 2023. Tree health condition in Urban Green Areas assessed through crown indicators and vegetation indices. Forests 14 (8), 1673. http://dx.doi.org/10.3390/f14081673.

Muliady., M., Lim., T.S., Koo., V.C., Winata., N.P., 2022. Estimation of paddy leaf nitrogen status using a single sensor multispectral camera. In: Proceedings of the 1st International Conference on Emerging Issues in Technology, Engineering and Science - ICE-TES. pp. 26–31. http://dx.doi.org/10.5220/0010743900003113.

Näsi, R., Honkavaara, E., Blomqvist, M., Lyytikäinen-Saarenmaa, P., Hakala, T., Viljanen, N., Kantola, T., Holopainen, M., 2018. Remote sensing of bark beetle damage in urban forests at individual tree level using a novel hyperspectral camera from UAV and aircraft. Urban For. Urban Green. 30, 72–83. http://dx.doi.org/10.1016/j.ufug.2018.01.010, URL https://www.sciencedirect.com/science/article/pii/S1618866716305581.

Nireos, 2025. HERA VNIR hyperspectral camera. URL https://nireos.com/product/hera-vnir/.

Nowak, D.J., Greenfield, E.J., 2018. Declining urban and community tree cover in the United States. Urban For. Urban Green. 32, 32–55. http://dx.doi.org/10.1016/j.ufug.2018.03.006.

Nowak, D.J., Hirabayashi, S., Bodine, A., Greenfield, E., 2014. Tree and forest effects on air quality and human health in the United States. Environ. Pollut. 193, 119–129. http://dx.doi.org/10.1016/j.envpol.2014.05.028.

Numba Developers, 2025. Numba: A Just-In-Time compiler for numerical Python. URL https://numba.pydata.org.

NumPy Developers, 2025. NumPy: The fundamental package for scientific computing with Python. URL https://numpy.org.

OpenCV Team, 2025. OpenCV: Open source computer vision library. URL https://opencv.org.

Padshetty, S., Ambika, 2023. Leaky ReLU-ResNet for plant leaf disease detection: A deep learning approach. Eng. Proc. 59 (1), http://dx.doi.org/10.3390/engproc2023059039, URL https://www.mdpi.com/2673-4591/59/1/39.

Pix4D S.A., 2025. PIX4Dfields: Drone software for agriculture mapping. https://www.pix4d.com/product/pix4dfields/. (Accessed 29 April 2025).

Python Software Foundation, 2023. Python programming language. URL https://www.python.org.

QGIS Development Team, 2024. QGIS geographic information system. https://www.qgis.org.

Raspberry Pi Ltd, 2025. Raspberry Pi 4 model B. URL https://www.raspberrypi.com/products/raspberry-pi-4-model-b/.

Reyes-Riveros, R., Altamirano, A., De La Barrera, F., Rozas-Vásquez, D., Vieli, L., Meli, P., 2021. Linking public urban green spaces and Human Well-Being: A systematic review. Urban For. Urban Green. 61, 127105. http://dx.doi.org/10.1016/j.ufug.2021.127105.

Stuart, M.B., Davies, M., Hobbs, M.J., McGonigle, A.J.S., Willmott, J.R., 2022. Peatland plant spectral response as a proxy for peat health, analysis using low-cost hyperspectral imaging techniques. Remote. Sens. 14 (16), 3846. http://dx.doi.org/10.3390/rs14163846.

Torresan, C., Benito Garzón, M., O'Grady, M., Robson, T., Picchi, G., Panzacchi, P., Tomelleri, E., Smith, M., Marshall, J., Wingate, L., Tognetti, R., Rustad, L., Kneeshaw, D., 2021. A new generation of sensors and monitoring tools to support climate-smart forestry practices. J. Can. J. For. Res. 51 (12), 1751–1765. http://dx.doi.org/10.1139/cjfr-2020-0295.

Viecco, M., Vera, S., Jorquera, H., Bustamante, W., Gironás, J., Dobbs, C., Leiva, E., 2018. Potential of particle matter dry deposition on green roofs and living walls vegetation for mitigating urban atmospheric pollution in semiarid climates. Sustainability 10 (7), 2431. http://dx.doi.org/10.3390/su10072431.

Wang, A., Machida, Y., deSouza, P., Mora, S., Duhl, T., Hudda, N., Durant, J.L., Duarte, F., Ratti, C., 2023a. Leveraging machine learning algorithms to advance Low-Cost air sensor calibration in stationary and mobile settings. Atmos. Environ. 301, 119692. http://dx.doi.org/10.1016/j.atmosenv.2023.119692.

Wang, A., Paul, S., deSouza, P., Machida, Y., Mora, S., Duarte, F., Ratti, C., 2023b. Key themes, trends, and drivers of mobile ambient air quality monitoring: A systematic review and Meta-Analysis. Environ. Sci. Technol. 57 (26), 9427–9444. http://dx.doi.org/10.1021/acs.est.2c06310, arXiv:https://doi.org/10.1021/acs.est.2c06310 PMID: 37343238.

Wang, J., Zhen, Z., Zhao, Y., Ma, Y., Zhao, Y., 2024. 3D-CNN with Multi-Scale fusion for tree crown segmentation and species classification. Remote. Sens. 16 (23), http://dx.doi.org/10.3390/rs16234544, URL https://www.mdpi.com/2072-4292/16/23/4544.

Xue, J., Su, B., 2017. Significant remote sensing vegetation indices: A review of developments and applications. J. Sens. 2017, 1–17. http://dx.doi.org/10.1155/2017/1353691.

Zhang, L., Wang, L., Wu, J., Li, P., Dong, J., Wang, T., 2023. Decoding urban green spaces: Deep learning and google street view measure greening structures. Urban For. Urban Green. 87, 128028. http://dx.doi.org/10.1016/j.ufug.2023.128028.

Zhou, B., Zhao, H., Puig, X., Fidler, S., Barriuso, A., Torralba, A., 2017. Scene parsing through ADE20K dataset. In: 2017 IEEE Conference on Computer Vision and Pattern Recognition. CVPR, pp. 5122–5130. http://dx.doi.org/10.1109/CVPR.2017.544.

Ziter, C.D., Pedersen, E.J., Kucharik, C.J., Turner, M.G., 2019. Scale-dependent interactions between tree canopy cover and impervious surfaces reduce daytime urban heat during summer. Proc. Natl. Acad. Sci. 116 (15), 7575–7580. http://dx.doi.org/10.1073/pnas.1817561116.